



Effect of electrode compression on the wettability of lithium-ion batteries



Sang Gun Lee^a, Dong Hyup Jeon^{b,*}

^aSchool of Mechanical and Aerospace Engineering, Seoul National University, Seoul 151-742, Republic of Korea

^bDepartment of Mechanical System Engineering, Dongguk University-Gyeongju, 123 Dongdae-ro, Gyeongju 780-714, Gyeongsangbuk, Republic of Korea

HIGHLIGHTS

- We simulate electrolyte transport dynamics in the compressed electrode of LIB.
- The anode has lower wettability than the cathode.
- The particle shape has a strong effect on the wettability.

ARTICLE INFO

Article history:

Received 7 March 2014

Received in revised form

21 April 2014

Accepted 25 April 2014

Available online 9 May 2014

Keywords:

Wettability

Lithium-ion batteries

Lattice Boltzmann method

Electrode compression

Electrolyte saturation

ABSTRACT

Using the multiphase lattice Boltzmann method (LBM), the electrolyte transport dynamics in the two-dimensional electrode structure of a lithium-ion battery are simulated. The effect of the compression ratio of a porous electrode on wettability is explored with respect to variations of porosity and particle shape. The electrolyte distribution in the electrode and the electrolyte saturation profile are examined in order to evaluate the wetting capability at various compression ratios. The results show that wettability in the electrode decreases as the compression ratio increases. In a highly compressed electrode, the through-plane permeation of liquid electrolyte is small. Thus, the electrolytes are mainly observed at the interface of the electrode and separator. The anode has lower wettability than the cathode due to the deformation of particle shape during the manufacturing process. Therefore, particle shape has a strong effect on wettability. The two-dimensional LBM approach used in this study characterizes the electrolyte transport phenomena inside the electrode and allows us to compare the wettability between the cathode and anode at various compression ratios.

© 2014 Elsevier B.V. All rights reserved.

1. Introduction

The wetting capability of an electrolyte is a critical issue for the commercialization of lithium-ion batteries (LIBs) in electric vehicle (EV) and hybrid electric vehicle (HEV) applications. The electrode needs to be fully wetted with the electrolyte to maintain high utilization of electrode capacity. Insufficient electrolyte wetting in the electrode causes irregular reactions of the electrochemistry, and deteriorates LIB performance. This phenomenon causes extrusion of lithium metal that may result in a serious problem in relation to the safety issue. Moreover, inferior wetting with the electrolyte accelerates the degradation of LIBs, resulting in a shortened cycle life.

Recent research efforts for EV and HEV applications have considered high energy and high power densities. According to the United States Advanced Battery Consortium (USABC), long term goals for energy and power densities are 300 Wh/L and 600 W/L, respectively [1]. To achieve these goals, a high packing density of the electrode is necessary. On the other hand, this may lead to insufficient electrolyte wetting in the electrode by lowering the porosity and increasing pore blockage. Yu et al. [2] suggested that thick and dense electrodes degrade discharge capacity rapidly at high current rates. This is believed to be due to the insufficient wetting in the electrode caused by high packing density. The main objective of the present study is to investigate the effect of electrode compression on the wettability in the electrodes.

A number of experiments have been conducted regarding wettability in batteries. Wu et al. [3] investigated the wettability in the electrodes of an LIB. Their experimental results showed that an increase in surface tension reduces electrolyte spreading in the

* Corresponding author. Tel.: +82 54 770 2209; fax: +82 54 770 2282.

E-mail address: jeondh@dongguk.ac.kr (D.H. Jeon).

pores. They reported that the wetting in the electrode depends on electrolyte penetration and spreading which are determined by viscosity and surface tension. Zguris [4] and Culpin [5] examined the wettability of the separator for valve-regulated lead/acid (VRLA) batteries. They suggested that the fluid absorption properties of the separator are an important battery design consideration. Manev et al. [6] examined that the effect of preliminary treatment and technique on the charge/discharge behavior of graphite. They reported that a higher compacting pressure on the electrode leads to a decrease in the specific capacity. Chu et al. [7] investigated that the influence of compaction on the porosity and electrochemical properties of positive electrode. They suggested that the wettability is predominant at high C rate along with densification. Although many efforts have been made regarding wettability, no *in-situ* visualization method has been reported that can detect the electrolyte distribution inside the electrode. More recently, Lee et al. [8] identified the wetting mechanism in the porous electrode of an LIB using the two-dimensional lattice Boltzmann method (LBM). They demonstrated the dynamic behavior of the liquid electrolyte in a porous electrode as well as wetting phenomena in a microstructure. Their results demonstrated that the LBM can be effectively used to estimate the liquid electrolyte behavior in a porous electrode by giving a realistic pore-scale dynamic simulation.

The LBM has been widely used to study the viscous coupling effects in immiscible two-phase flow in porous media. Unlike the traditional computational fluid dynamics (CFD) method which solves the Navier–Stokes equation at a macroscopic scale, the LBM simulates fluid flows by tracking the evolution of a single-particle distribution. The LBM is computationally accurate and efficient method. Due to this characteristic, the LBM can separate the immiscible fluids without tracking interfaces while sharp interfaces are maintained automatically. Therefore, the LBM can be applied successfully to simulate immiscible flows such as bubble collision and rising, and wetting and spreading phenomenon. The LBM is a parallel method because all the information transfer is local in time and space [9,10]. Using modern computers with massively parallel processors, the LBM has become a promising computational method for studying various complex systems [11].

This paper develops a numerical simulation using the LBM to investigate the effects of the compression ratio (CR) on wettability. The two-phase intermolecular potential model proposed by Shan and Chen [9,10] was used to examine the microscopic behavior occurring at the pore scale in a complex porous structure. Based on our previous work [8] in which the wetting mechanism in a porous electrode was investigated, the present study extends the wetting phenomena in both the cathode and anode by considering various compression ratios. The changes of particle shape are taken into consideration in the anode, because the anode material can undergo plastic deformation during the manufacturing process. Cross-sectional liquid electrolyte distribution and saturation profiles are presented. This study focuses on a comparison of wetting capability between the cathode and anode.

2. Model description

2.1. LBM model

The LBM originated from lattice gas automata (LGA) and is numerically derived from the continuous Boltzmann equation discretized in time and phase space [12]. In the LBM, the particle population in the LGA model is replaced by the distribution function. The time variation of the distribution functions is calculated by performing simple law of collision and streaming steps. In this study, we implemented the lattice Bhatnagar–Gross–Krook (LBGK)

model for the collision term approximation. The discrete particle distribution functions f_i are written as

$$f_i(\mathbf{x} + \mathbf{e}_i \Delta t, t + \Delta t) = f_i(\mathbf{x}, t) - \frac{\Delta t}{\tau} [f_i(\mathbf{x}, t) - f_i^{\text{eq}}(\mathbf{x}, t)] + S_i(\mathbf{x}, t) \quad (1)$$

where $f_i(\mathbf{x}, t)$ is the probability of finding a particle in the i th velocity \mathbf{e}_i at (\mathbf{x}, t) , and Δt is the time step. τ is the dimensionless relaxation time that is related to the kinetic viscosity ν and controls the tendency of the system to relax the local equilibrium. $S_i(\mathbf{x}, t)$ is a source term added to the standard lattice Boltzmann equation. Various fluid dynamics phenomena can be expressed by using different forms of the source terms. f_i^{eq} is the equilibrium distribution function which is a specially discretized Maxwell–Boltzmann function with a Taylor expansion [12] and is given as follows:

$$f_i^{\text{eq}} = \rho w_i \left(1 + \frac{\vec{e}_i \cdot \vec{u}^{\text{eq}}}{c_s^2} + \frac{(\vec{e}_i \cdot \vec{u}^{\text{eq}})^2}{2c_s^4} - \frac{(\vec{u}^{\text{eq}})^2}{2c_s^2} \right) \quad (2)$$

where c_s is the speed of sound in a liquid electrolyte which is $c/3$; c denotes the ratio of lattice space to the time step, which is $c = \Delta x / \Delta t$; and w_i is the weight factor, which is $4/9$ for $i = 1$, $1/9$ for $i = 2, 3, 4, 5$ and $1/36$ for $i = 6, 7, 8, 9$. In this study, two-dimensional nine velocities (D2Q9) model was used on the two-dimensional square lattice as shown in Fig. 1. By applying the D2Q9 model, the discrete velocity \mathbf{e}_i can be written as

$$[\mathbf{e}_1, \mathbf{e}_2, \mathbf{e}_3, \mathbf{e}_4, \mathbf{e}_5, \mathbf{e}_6, \mathbf{e}_7, \mathbf{e}_8, \mathbf{e}_9] = \begin{bmatrix} 0 & 1 & 0 & -1 & 0 & 1 & -1 & -1 & -1 \\ 0 & 0 & 1 & 0 & -1 & 1 & 1 & -1 & -1 \end{bmatrix} \quad (3)$$

In a Newtonian fluid, the fluid density ρ and equilibrium velocity \mathbf{u}^{eq} can be calculated using the following equations:

$$\rho = \sum_{i=1}^9 f_i \quad (4)$$

$$\mathbf{u}^{\text{eq}} = \mathbf{u} + \frac{\tau \mathbf{F}}{\rho} \quad (5)$$

where \mathbf{u} is a local velocity given by $\mathbf{u} = \sum_a f_a \mathbf{e}_a / \rho$. \mathbf{F} is the total force acting on the fluid that is comprised of inter-particle force \mathbf{F}_{int} , adhesion force \mathbf{F}_{ads} between a liquid and gas with a solid phase, and external force \mathbf{F}_{ext} . In this study, it is assumed that \mathbf{F}_{ext} has a uniform value in a steady body. \mathbf{F}_{int} and \mathbf{F}_{ads} were calculated using the following equations:

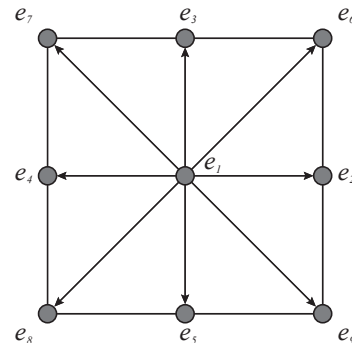


Fig. 1. Lattice structure of two-dimensional nine velocity (D2Q9) model.

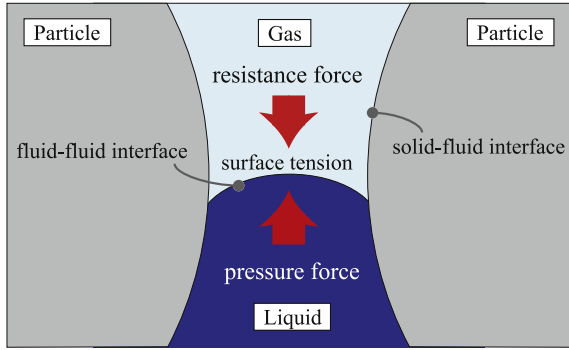


Fig. 2. Schematic of phase interfaces.

$$\mathbf{F}_{\text{int}}(\mathbf{x}, t) = -G\psi(\mathbf{x}, t) \sum_{i=1}^9 w_i \psi(\mathbf{x} + \mathbf{e}_i \Delta t, t) \mathbf{e}_i \quad (6)$$

$$\mathbf{F}_{\text{ads}}(\mathbf{x}, t) = -G\psi(\rho(\mathbf{x}, t)) \sum_{i=1}^9 w_i \psi(\rho(x_w)) s(\mathbf{x} + \mathbf{e}_i \Delta t, t) \mathbf{e}_i \quad (7)$$

where G is Green's function, which controls the strength of the interparticle-force, and the signs of G determines whether it is attractive or repulsive [8]. ψ is a function of density in the following empirical form: $\psi(\rho) = \rho_0[1 - \exp(-\rho/\rho_0)]$, where ρ_0 is constant. s is an indicator function: 1 for a solid domain node and 0 for a fluid domain node. $\rho(x_w)$ is the density of solid phase, and provides a free parameter with which to tune different wall properties independently from the real density value. The desired contact angle can be derived by controlling the value of $\rho(x_w)$ [13]. This allows the different contact angles for various wall conditions to be easily imported.

This proposed model adopts the Shan-Chen pseudo-potential model which is one of the most popular multiphase models. The pseudo-potential model allows the separation of two immiscible fluids if the interaction force between the fluids is larger than a threshold value. The multiphase interface includes fluid–fluid interface and fluid–solid interface as shown in Fig. 2. A fluid–fluid interface is formed between the two immiscible fluids and fluid–solid interface is formed between fluid and solid. According to

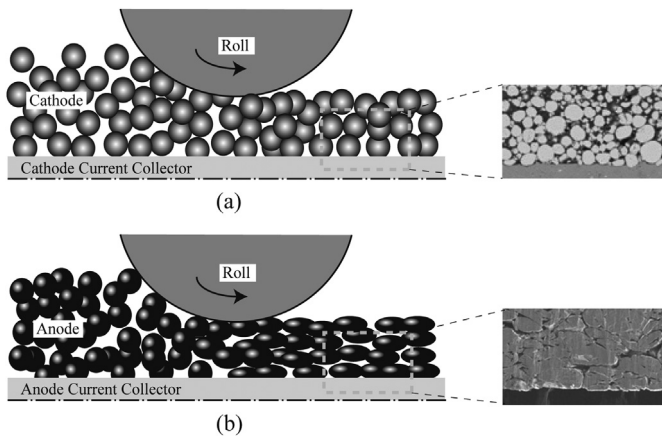


Fig. 3. Schematic of roll pressing process for (a) cathode and (b) anode electrodes. The corresponding images of the particle are presented. Note that the cathode particles maintain spherical shape, whereas the anode particles are deformed to elliptic shape after roll pressing process.

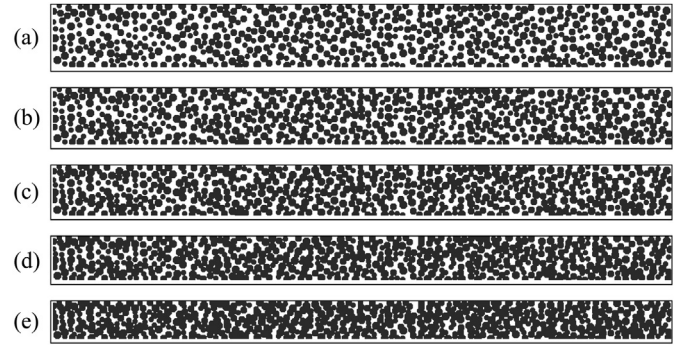


Fig. 4. Reconstruction of cathode electrodes when the compression ratios are (a) 0%, (b) 10%, (c) 20%, (d) 30% and (e) 40%.

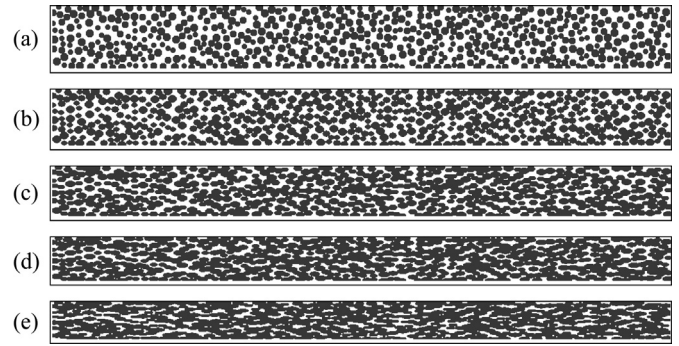


Fig. 5. Reconstruction of anode electrodes when the compression ratios are (a) 0%, (b) 10%, (c) 20%, (d) 30% and (e) 40%. The deformation of particles is considered.

Srivastava et al. [14], the Shan-Chen multiphase model and the multi-component LBM model shows good agreement with the sharp interface model.

2.2. Reconstruction of porous electrodes

The commercially available cathode materials are LiCoO_2 (LCO), LiMn_2O_4 (LMO), $\text{Li}(\text{NiCoMn})\text{O}_2$ (NCM) and LiFePO_4 (LFP). These materials are ceramics, which are hard and strong in compression.

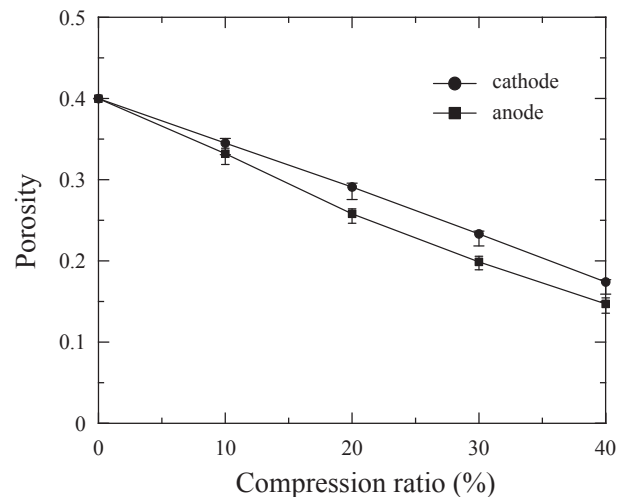


Fig. 6. Predicted porosity at various compression ratios with error bars which represent standard deviation.

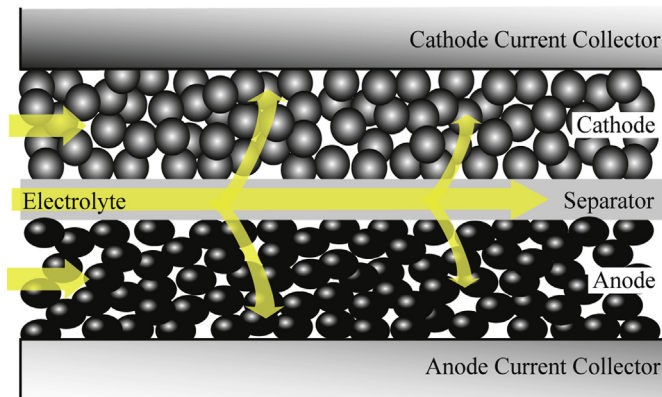


Fig. 7. Schematic of electrolyte filling process in a unit cell.

On the other hand, graphite which is the most popular anode material undergoes plastic deformation during the roll-pressing process as shown in Fig. 3. Scanning electron microscopy (SEM) images of the cathode and anode were taken after compression, and are shown in Fig. 3. SEM examination shows that the cathode particles maintained a spherical shape, whereas the anode particles deformed to an elliptical shape which corresponds to the results of Wang et al. [15]. Therefore the deformation of anode particle should be taken into consideration for the simulation of wettability in a compressed anode.

For the reconstruction of porous electrodes, it is assumed that the electrode consists of randomly packed spherical particles at arbitrary positions. The structure of the porous electrode is constructed with impermeable solid particles and pore areas. Spherical particles are generated with a prescribed radius and porosity. Since the newly generated particle can take its position close enough to a pre-existing neighborhood, overlapping between the particles is allowed. Therefore, the actual porosity in the numerical domain is determined by the ratio of the number of void grid lattices to the number of grid lattices. It is assumed that compression force does not destroy the solid particles, but merely reduces the pore space. Based on these assumptions, the microstructure of both the cathode and anode are constructed as shown in Figs. 4 and 5. Figs. 4(a) and 5(a) show the uncompressed electrodes, which are used as a baseline. Four different compression ratios (10%, 20%, 30%, and 40%) were taken into consideration at the cathode and anode electrodes. As the compression progress, the volume of the particle is conserved, whereas that of the void space is reduced. This indicates a decrease in the porosity. As previously mentioned, the particle shape at the cathode remains spherical because cathode materials are strong in compression, and the particle shape at the anode becomes elliptical due to plastic deformation. In the compressed anode, spherical particles are compressed in a through-plane direction and extended in an in-plane direction.

Fig. 6 shows the porosity changes in the cathode and anode for various compression ratios. Because the initial porosity was set to 0.4, the porosity is expected to be zero when the compression ratio is over 40%. On the other hand, the predicted porosity is greater than zero. This is because the reconstruction is made in the two-dimensional domain by allowing an overlap between the particles. For the sake of clarity, corresponding error bars are shown in

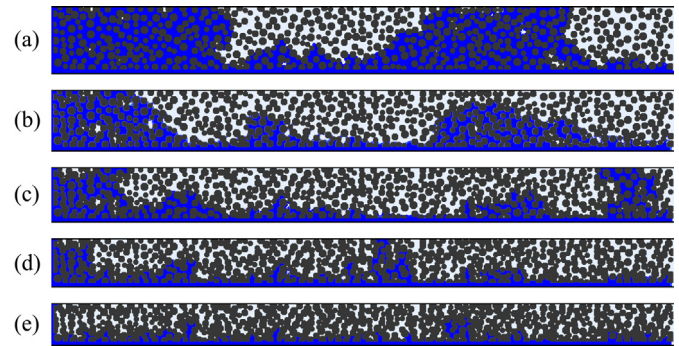


Fig. 9. Liquid electrolyte distribution in the cathode when the compression ratios are (a) 0%, (b) 10%, (c) 20%, (d) 30% and (e) 40%.

Fig. 6. The figure shows that the porosity in the cathode is larger than that in the anode. This is due to the particle shape, which remained spherical in the cathode, but deformed to an elliptical shape in the anode. From a geometric point of view, the void space between the spherical particles is greater than the void space between the elliptic particles.

2.3. Numerical procedure

The electrolyte filling process in a unit cell, i.e., cathode, anode, separator, cathode current collector and anode current collector, is shown in Fig. 7. Based on results reported in Ref. [7], the wetting mechanism is described as follows. First, the electrolytes are transported from the inlet at the beginning of the process. Second, the inflowing electrolytes penetrate through the porous electrodes and separator due to capillary pressure. Third, the electrolytes spread into the electrodes from the separator because the electrolyte transportation in the separator is faster than that in the electrodes. To simulate liquid electrolyte transport in a porous electrode, a lattice Boltzmann (LB) model was developed as shown schematically in Fig. 8. To simplify the LB simulation, the computational domain consists of an electrode and a separator. The two-dimensional domain size is $1000 \times 105 \text{ lu}^2$ including a porous electrode of $1000 \times 100 \text{ lu}^2$ and a separator of $1000 \times 5 \text{ lu}^2$ (lu: lattice unit, 1 lu means $1 \mu\text{m}$ of the physical length in this study). It is assumed that the electrode is comprised of impermeable solid particles and pore areas, and the separator is comprised of highly porous material. The boundary conditions proposed by Zou and He [16], who implemented no-slip bounce back condition on the walls, are applied. The inlet condition was set on the left boundary with an inflowing velocity of $7.0 \times 10^{-5} \text{ lu}$. The resulting Reynolds and capillary numbers are 0.005 and 8.33×10^{-6} , respectively. A fixed pressure condition was applied at the right boundary and the top and bottom boundaries were set to a no-slip condition. The bounce back condition, i.e., the incoming distribution function is simply equal to the corresponding outgoing distribution function with an opposite momentum, was imposed at the top and bottom walls. A porosity of 0.4 and a particle radius of 5–7 lu were used as initial values for the simulation of the uncompressed electrode. Since the roughness can change the contact angle of particle surface, the neutral wetting case with a contact angle of 90° was considered in the present study. The finer time step and grid size ensure better

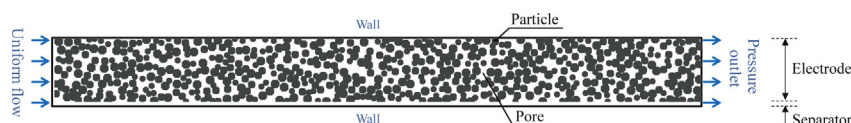


Fig. 8. Computational domain of two-dimensional LB model with boundary conditions.

convergence and accuracy, but they incur a high calculation cost. The appropriate time step ($\Delta t = 1$ lu) and grid size ($\Delta x = 1$ lu) were selected by considering the motion of the liquid electrolyte and gaseous air. The computational time for this calculation was about 4.3×10^5 s per 9×10^7 time steps on 12 nodes of parallel processors using the Linux operating system with a 3.30 GHz clock speed. The validation for the present LB model was reported in our previous paper [8], so it will not be repeated here.

3. Results and discussion

3.1. Wettability in the cathode

Fig. 9 shows the liquid electrolyte distribution in the cathode. Five different compression ratios (0%, 10%, 20%, 30% and 40%) are considered for a lattice time of 6.0×10^7 lu. Since the electrolyte distribution did not show any difference after this time, the calculation was assumed to have converged. To relate the physical space to the lattice space, a time step of $\Delta t = 6.67 \times 10^{-10}$ is chosen. In this figure, the blue and light gray represent the liquid electrolyte and gaseous air, respectively. The liquid electrolyte driven by constant velocity at the inlet pushes gaseous air toward the outlet. The electrolyte transport is due to the interplay among three forces: the pressure force $F_p = -\Delta p A$ from the connecting electrolytes, the capillary force from the surface tension $F_s = -\sigma \pi d$, and the resistance force F_R from the existing air in the pores. As a result, the air moves driven by the flow motion of the electrolyte. A more detailed wetting mechanism can be found in our previous paper [8]. The results of the present study show that the higher compression ratio decreases the electrolyte distribution caused by lower porosity. In Fig. 9(a) which shows an uncompressed cathode, the electrolytes are distributed in large areas. Two main streams are observed which are transported by the insertion of the flow from the inlet and the integration of the flow paths spread from the separator. These are distributed mainly at the inlet and the bottom of the cathode. Gaseous air is observed in the middle and at the outlet. The former is trapped by the electrolyte and the latter obstructs the flow path. Fig. 9(b) shows a 10% compressed cathode, and the area of liquid electrolyte is decreased by a reduction in the pore of the infiltrated flow paths. Most flow paths that are spread from the separator do not reach the top. This is attributed to the blockage of the flow paths and the resistance force. Fig. 9(c) and (d) shows that the area of liquid electrolyte is reduced significantly

and the electrolyte distribution is changed when compared to Fig. 9(a) and (b). This is because the electrolytes selected another preferential path, which is caused by an increased resistance force. In Fig. 9(e) which shows a 40% compressed cathode, the electrolytes are observed mainly at the bottom and are rarely found at the top. This is due to the increasing number of disconnected pore throats resulting from the blockage of particles and smaller pores. This indicates that the electrolytes permeate slightly into the pores in a highly compressed cathode.

Fig. 10 shows the variations of liquid electrolyte saturation in the cathode along the lattice time. A comparison is made with various compression ratios. The electrolyte saturation is measured using the ratio of liquid electrolyte area to the pore space area. As the lattice time increases, electrolyte saturation increases rapidly until a certain lattice time, and then the gradient decreases. When the cathode is uncompressed, the electrolyte saturation increases steadily due to the creation of penetration paths and the extension of the paths into the pores. The uncompressed cathode presents the highest electrolyte saturation. When the compression ratio is 10%, 20% and 30%, the electrolyte saturations decrease by approximately 30–50% with a gradual gradient. This indicates that the electrolyte has several penetration flow paths, and thus the electrolyte transport proceeds slowly despite the increased resistance force. The electrolyte saturation has several irregular slopes at 1.4×10^7 and 2.2×10^7 lu for CR = 10%; 0.7×10^7 and 3.4×10^7 lu for CR = 20%; and 0.5×10^7 lu and 4.3×10^7 lu for CR = 30%. This is because the flow found a new path and squeezed the electrolyte into the pores. When the compression ratios are 40%, the electrolyte saturation is reduced significantly and converges in the early stage, indicating that there are limited penetration flow paths in the cathode.

Fig. 11 shows the liquid electrolyte saturation profile along the cathode thickness. The electrolyte saturation is compared with various compression ratios. This figure shows that the electrolyte saturation decreases along the thickness. The electrolyte saturation is observed to be high at the bottom, but this becomes lower along the thickness. The uncompressed cathode has a comparatively linear decrease along the thickness, whereas the compressed cathode presents a sharp drop near the bottom. Because the highly compressed cathode has a high resistance force, it is reasonable to expect lower wettability with an increasing compression ratio. The irregular slope is caused by non-uniform air distribution that is trapped inside the cathode. The electrolyte saturation of an

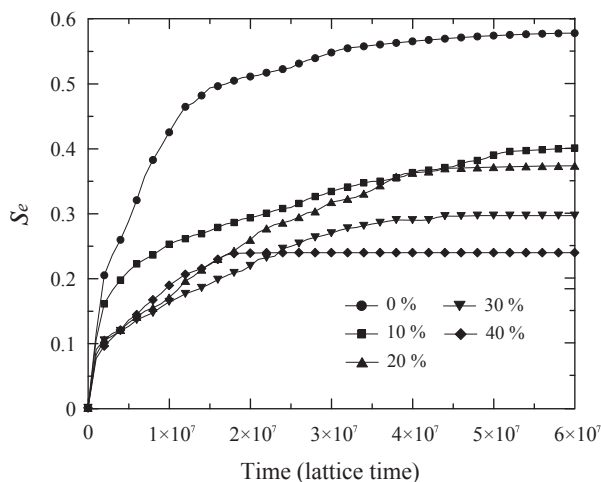


Fig. 10. Transient saturation profile of liquid electrolyte in the cathode with various compression ratios.

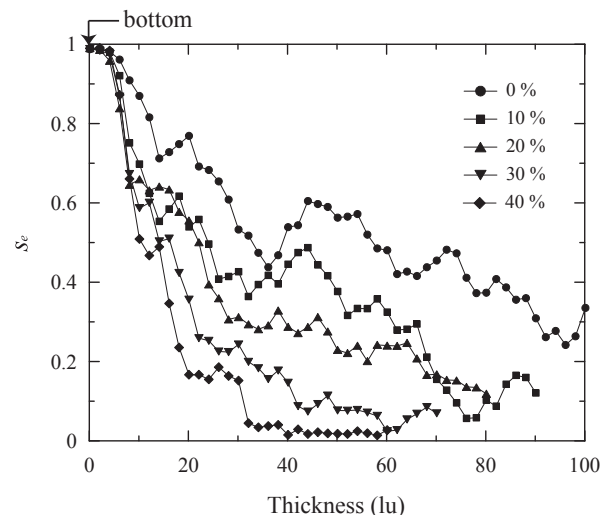


Fig. 11. Liquid electrolyte saturation profile along the cathode thickness.

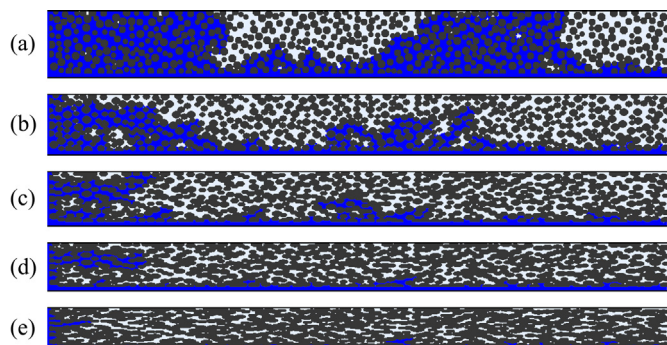


Fig. 12. Liquid electrolyte distribution in the anode when the compression ratios are (a) 0%, (b) 10%, (c) 20%, (d) 30% and (e) 40%.

uncompressed cathode is approximately 30% at the top. On the other hand, the compressed cathode presents low electrolyte saturation in this region which is attributed to the electrolyte penetration from the inlet. This indicates that the electrolyte flow paths from the separator can hardly reach the top in a highly compressed cathode. This result confirms that the thick cathode with high compression ratio can lead to low utilization of the cathode due to a low wetting capability.

3.2. Wettability in the anode

Fig. 12 shows the liquid electrolyte distribution in the anode when the lattice time is 6.0×10^7 lu. For comparison with electrolyte distributions in the cathode, the same compressing conditions were applied. Fig. 12(a) presents the electrolyte distribution in an uncompressed anode which is used as a baseline. Fig. 12(b), (c) and (d) shows the electrolyte distribution for compression ratios of 10%, 20% and 30%, respectively. Compared to the plots shown in Fig. 9, the through-plane permeation of the liquid electrolyte decreased and the flow paths of the branches changed their direction due to particle deformation. Because the particles are compressed in a through-plane direction and are expanded in an in-plane direction, the in-plane pore size is reduced. Since creeping flow through a small pore is dominantly influenced by capillary pressure, and since the electrolyte selects a relatively wide throat, the infiltrated flow path stretches to the in-plane direction rather

Table 1

Predicted result of liquid electrolyte saturation.

CR	0%	10%	20%	30%	40%
Cathode	57.8	40	37.3	29.6	23.9
Anode	57.8	34.3	26.4	19.9	13.4

than the through-plane direction. These phenomena can be clearly seen in Fig. 12(e) which shows the electrolyte distribution when the compression ratio is 40%. Because the compression ratio is significantly high, pore sizes are substantially reduced and many pore paths are blocked by the particles. As a result, most electrolytes are observed near the bottom.

Fig. 13 shows variations of liquid electrolyte saturation in the anode along the lattice time. As the compression ratio increases, the electrolyte saturation decreases. When the compression ratio is 10%, the electrolyte saturation is reduced to one-half in comparison with the uncompressed anode. This is attributed to a decrease in the through-plane flow path. When the compression ratios are 20% and 30%, the electrolyte saturation increases rapidly at 2.0×10^7 and 3.2×10^7 , respectively. This is due to the squeezing of the electrolyte that found a new path in the pores, as previously described. When the compression ratio is 40%, the electrolyte saturation is reduced significantly and converges in the early stage. This is caused by a high compression ratio that gives limited invasion routes, and thus the flow path could not find the linked throat to penetrate into the pores. Comparing the cathode and anode, the cathode has higher electrolyte saturation than the anode at each compression ratio, as shown in Table 1. Considering that the porosity of the anode is slightly lower than that of the cathode as shown in Fig. 6, it can be concluded that the effect of particle shape is significant.

Fig. 14 shows the liquid electrolyte saturation profile along the anode thickness. The electrolyte saturation is decreased along the anode thickness. The electrolyte saturation of compressed anodes decreases rapidly near the bottom of electrode. This increases slightly at 30 lu, and drops thereafter. The increase of the electrolyte saturation in this region is due to electrolyte intrusion from the inlet that is not spread from the separator, as shown in Fig. 12. For all the compressed anodes, the electrolyte paths from the separator do not reach the top. This suggests that the resistance force is very high in a through-plane direction. Compared to the electrolyte

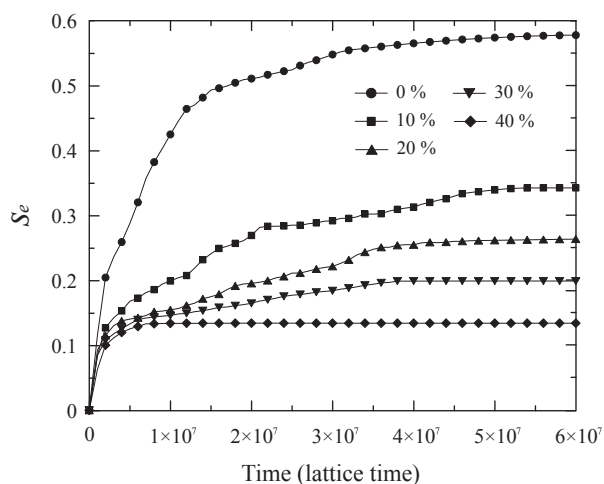


Fig. 13. Transient saturation profile of liquid electrolyte in the anode with various compression ratios.

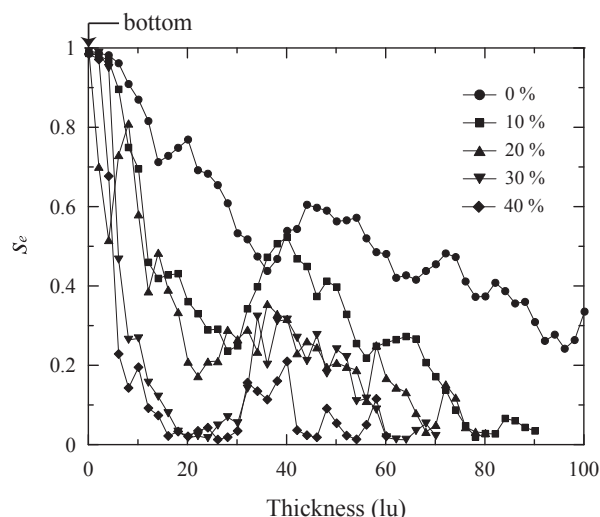


Fig. 14. Liquid electrolyte saturation profile along the anode thickness.

saturation profile in the cathode shown in Fig. 11, the electrolyte transport in an in-plane direction is increased, whereas that in a through-plane direction is decreased.

The simulation results confirm that the compression ratio significantly affects electrolyte penetration into a porous anode, and suggest that the particle shape is important for the electrolyte penetration in the anode. This further suggests that a thin anode is favorable for an electrode design with high packing density.

4. Conclusion

The wettability of the cathode and anode has been investigated using two-dimensional LBM simulation. The LB model was developed to simulate the effect of the compression ratio on wettability. The reconstruction of spherical particles in the cathode and elliptical particles in the anode was established by assuming that the cathode materials are strong in compression and the anode materials undergo plastic deformation. This model enables us to visualize the electrolyte penetrating process through micro-pores, and compare the wetting capability between the cathode and anode. It should be noted that the electrolyte transport through the front and back was not considered due to the limitations of two-dimensional simulation developed in this work. Extension of the model to three-dimensional may improve the accuracy, but this is beyond the scope of this study. The results show that the effect of the compression ratio on wettability is significant. The area of liquid electrolyte in the compressed electrodes is reduced compared to uncompressed electrodes. As the compression ratio increases, the wetting capability is decreased. Because the anode particles have a through-plane compression and in-plane expansion, the through-plane permeation of liquid electrolyte decreases. This causes a lower wetting capability in the anode, which results in low utilization of the anode. On the other hand, the cathode particles maintain a spherical shape as the compression progresses. This merely decreases the porosity by providing an environment such that infiltrated flow paths can easily spread from the separator and penetrate in a through-plane direction. This suggests that the effect of particle shape on wettability is significant.

The results of the present study provide a mechanism for electrolyte transport in a compressed electrode. The electrolyte transports into the porous electrode via two major paths: flow from the inlet and spread from the separator. Both paths depend on the pore size. Spread from the separator strongly depends on the particle shape. Considering that the size of an EV or HEV battery is very large, spread from the separator is more effective than flow from the inlet. Therefore careful control of the particle shape and electrode thickness is needed.

Acknowledgments

This work was supported by the National Research Foundation of Korea (NRF) grant funded by the Korea government (NRF-2013R1A1A2057761 and NRF-2013R1A1A2A10008883) and the Dongguk University Research Fund of 2013.

Nomenclature

A	area, m^2
Ca	capillary number
CR	compression ratio
C_s	speed of sound, m s^{-1}
d	pore diameter, m
\mathbf{e}_i	lattice velocity, m s^{-1}
f	distribution function
\mathbf{F}_{ads}	adhesion force
\mathbf{F}_{ext}	external force
\mathbf{F}_{int}	interparticle force
\mathbf{F}_p	pressure force
\mathbf{F}_r	resistance force
\mathbf{F}_s	capillary force from the surface tension
G	Green's function
S_e	electrolyte saturation
Δp	pressure difference, Pa
t	time, sec
u	velocity, m s^{-1}
w	weight coefficient
x	position coordinate, m

Greek letters

ν	kinetic viscosity, Pa s
σ	surface tension, N m^{-1}
ρ	density, kg m^{-3}
τ	relaxation time
ψ	function of density

Subscripts and superscripts

e	electrolyte
eq	equilibrium

References

- [1] NRC, Effectiveness of the United States Advanced Battery Consortium as a Government-industry Partnership, The National Academies Press, Washington, D.C., 1998.
- [2] S. Yu, T. Chung, M.S. Song, J.H. Nam, W.I. Cho, J. Appl. Electrochem. 42 (2012) 443.
- [3] M.-S. Wu, T.-L. Liao, Y.-Y. Wang, C.-C. Wan, J. Appl. Electrochem. 34 (2004) 797.
- [4] G.C. Zguris, J. Power Sources 88 (2000) 36.
- [5] B. Culpin, J. Power Sources 53 (1995) 127.
- [6] V. Manev, I. Naidenov, B. Puresheva, P. Zlatilova, G. Pistoia, J. Power Sources 55 (1995) 211.
- [7] C.-M. Chu, C.-Y. Liu, Y.-Y. Wang, C.-C. Wan, C.-R. Yang, J. Taiwan Inst. Chem. Eng. 43 (2012) 201.
- [8] S.G. Lee, D.H. Jeon, B.M. Kim, J.H. Kang, C.J. Kim, J. Electrochem. Soc. 160 (2013) H258.
- [9] X. Shan, H. Chen, Phys. Rev. E 47 (1993) 1815.
- [10] X. Shan, H. Chen, Phys. Rev. E 49 (1994) 2941.
- [11] X. He, L.-S. Luo, Phys. Rev. E 56 (1997) 6811.
- [12] S. Chen, G.D. Doolen, Annu. Rev. Fluid Mech. 30 (1998) 329.
- [13] R. Benzi, L. Biferale, M. Sbragaglia, S. Succi, F. Toschi, Phys. Rev. E 74 (2006) 021509.
- [14] S. Srivastava, P. Perlekar, L. Biferale, M. Sbragaglia, J.H.M. ten Thije Boonkamp, F. Toschi, Commun. Comput. Phys. 13 (2013) 725.
- [15] C.-W. Wang, Y.-B. Yi, A.M. Sastry, J. Shim, K.A. Striebel, J. Electrochem. Soc. 151 (2004) A1489.
- [16] Q. Zou, X. He, Phys. Fluids 9 (1997) 1591.